



Size distribution and particle morphology of analytes dried through the Evaporative Light Scattering Detector: Part A

Frederick Bertani¹, Joshua Hassim¹, and Simone Hochgreb¹

¹Department of Engineering, University of Cambridge, Trumpington Street, Cambridge, CB2 1PZ, UK

Correspondence: Simone Hochgreb (simone.hochgreb@eng.cam.ac.uk)

Abstract. This study investigates the size distribution and particle morphology of analytes dried through an Evaporative Light Scattering Detector (ELSD), a widely used detector based on aerosol light scattering in pharmaceutical and materials analysis. We employed multiple particle sizing techniques, including a Phase Doppler Particle Analyzer (PDPA), Aerodynamic Aerosol Classifier (AAC), and Scanning Mobility Particle Sizer (SMPS), to characterise droplet and particle distributions at various stages within the ELSD. Initial droplet size distributions were reconstructed using dioctyl sebacate (DOS) as a non-evaporating surrogate and correlated to water droplets. Downstream particle measurements were conducted for caffeine, dextran, and citric acid at different concentrations and operating conditions. Scanning Electron Microscopy (SEM) was used to examine dried particle morphology. Results show that analyte properties significantly influence final particle size and morphology, with implications for ELSD signal and detection detection. This is the first comprehensive characterisation of the particle drying and scattering process within an ELSD, and provides both physical insight in its operation, as well as data for the validation of a model.

1 Introduction

Analytical chemistry techniques often involve liquid chromatography for separation, followed by a detector for separate analytes. In many cases, the latter are detectable by UV or visible spectroscopy, but in many cases, analytes do not provide sufficient coupling signal, and other methods are required. The Evaporative Light Scattering Detector (ELSD) is one of the methods used for detection of such analytes commonly used in the pharmaceutical, bio-materials and food-manufacturing industry (Mourey and Oppenheimer, 1984). The eluent solution is atomised and passed through a heated tube, which removes the solvent and leaves behind dry analyte particles, which are then detected as light scattered by a laser beam (Lafosse et al., 1992). Thus, the ELSD is able to detect any analyte which is less volatile than its mobile phase, and it is commonly advertised as a 'universal detector', capable of detecting many species, including those that are not UV-Visible active.

Although the ELSD is a well-established analytical technique for analyte detection (Adelantado et al., 2016; Boborodea et al., 2018; Dalavitsou et al., 2019), the underlying physics of its operation remain poorly characterised. In particular, detailed data on particle transport—from atomisation through to detection—including processes such as impaction, diffusion, and evaporation, are absent from the literature.

https://doi.org/10.5194/ar-2025-35

Preprint. Discussion started: 18 November 2025

© Author(s) 2025. CC BY 4.0 License.





A number of studies have previously attempted to explore the dynamics of a solute-containing droplet through its lifetime, from the point of atomisation through to the dried particle, mostly exploring drying of metal compound solutions in spray drying applications (Urionabarrenetxea et al., 2021; Sungkhaphaitoon et al., 2017). Such studies use methods which include microscopy and sample collection onto a filter or a solid surface (Liu et al., 2019). However, there has yet to be an experimental investigation of the drying of particles in the particular situation of an organic low-volatility compound in a higher-volatility carrier. Studies which follow the life-time of an organic droplet in-situ with single-particle levitation techniques (electric-dynamic balance (Gregson et al., 2018), acoustic levitation (Doß and Bänsch, 2022; Fu et al., 2012; Wulsten et al., 2009), or optical tweezers Power and Reid (2014); Cai et al. (2015)) examine particles which are generally much larger (greater than 5μm) than relevant to the ELSD and generally have not explored the droplet from the point of atomisation.

The purpose of the present study is to obtain experimental results of particle size distributions relevant to the development of a model for the simulation of the signal obtained for the ELSD. The present work includes data from a variety of common organic compounds as analytes and investigates the drying process after injection through the ELSD under steady-state conditions for different temperatures and analyte concentrations.

In what follows, the methodology for the ELSD instrument is described, followed by a detailed overview of the analytical setup. A series of experimental configurations are employed to evaluate the atomised droplet size distribution, spanning from the submicron to the supermicron range. This broad size spectrum necessitates the use of multiple measurement techniques to bridge different size regimes reached by different instrumentation effectively. The dried analytes are subsequently characterised using an SMPS and Scanning Electron Microscope (SEM) to assess both particle size and morphology. The experimentally obtained dried particle size distributions serve as a benchmark for comparison with simulation results from a simplified numerical model presented in the companion paper (Bertani et al., 2025).

45 2 Methodology

50

2.1 Preparation of the analyte solutions

Caffeine, citric acid and dextran were chosen as analytes for this study. Caffeine was chosen because it is currently the standard default sample used in Agilent ELSDs as it is used for calibration. Dextran was chosen to represent a large molecular weight water-soluble polymer, as the ELSD is often used to analyse molecules of this type. Citric acid was chosen as a non-volatile non-cyclical small molecule alternative to caffeine. The properties of caffeine and citric acid are summarised below in Table 1. The properties of the variety of dextran used in this study are unknown to precise values, as they have not been tabulated by the manufacturer nor in the literature for such large molecular weight chains.

Solutions of aqueous caffeine (obtained from Alfa Aesar, Thermo Fisher Scientific), dextran (M_w = 450,000-650,000 g/mol; Scientific Laboratory Supplies Ltd.), and citric acid (Alfa Aesar, Thermo Fisher Scientific) were prepared using distilled water (Merck Life Science UK Ltd.) at concentrations of 0.125, 0.25, 0.5 and 1 g L⁻¹. After mixing, all solutions were sonicated in a water bath held at 25 °C for 10 minutes to ensure total dissolution.





Analyte	Mol. wt. $(gmol^{-1})$	Density (kgm ⁻³	$h_{lv} (\mathrm{kJkg}^{-1})$	p_v (Pa)
Caffeine	194	1230	345	9.8×10^{-3}
Citric Acid	192	1680	332	7.5×10^{-7}
Water	18	997	2255	3.2×10^{3}

Table 1. Analyte physico-chemical properties at 25 °C and atmospheric pressure, compared to those of water (Pence and Williams, 2010; Bothe and Cammenga, 1979; Griesser et al., 1999).

2.2 ELSD experimental setup

The ELSD (1290 Infinity II, Agilent Technologies) was operated at a steady-state liquid feeding rate, with the dissolved analyte in the mobile phase, instead of the more conventional analyte pulse injections from a liquid chromatography column. Steady-state operation is necessary to allow particle collection for SEM imaging and particle sizing experiments, which require significantly longer time scales than that of a pulsed injection. The ELSD was operated at a constant nebuliser temperature of 25 °C, an evaporator temperature of 25 °C, and a total gas flow rate of 2 L min⁻¹ of nitrogen (BOC Ltd.).

2.2.1 ELSD layout

The ELSD used in this study produces a spray using a twin-fluid coaxial Glass Expansion SeaSpray nebuliser. The volumetric gas flow rate going through the nebuliser is set by the manufacturer to a constant flow rate of 0.4 L min⁻¹ (Fig. 2). The detector unit itself has an internal geometric network of pipes as shown in the cross-sectional diagram in Figure 2. There are two possible points of impaction for the spray before it reaches the optical detection chamber; namely, the wall of the Y-junction after the atomisation chamber (marked (2)), and the plates of a diffuser cartridge beyond the Y-junction (at the interface between sections (3) and (4).

Figure 3 shows a schematic highlighting relevant sections of the ELSD which affect the total droplet count and size distribution, and thus the subsequent light-scattering response. These elements are to be characterised by particle concentration transfer functions.



Figure 1. a) SeaSpray high performance nebuliser, b) cross-sectional diagram of the nozzle tip showing liquid nozzle and gas annulus.





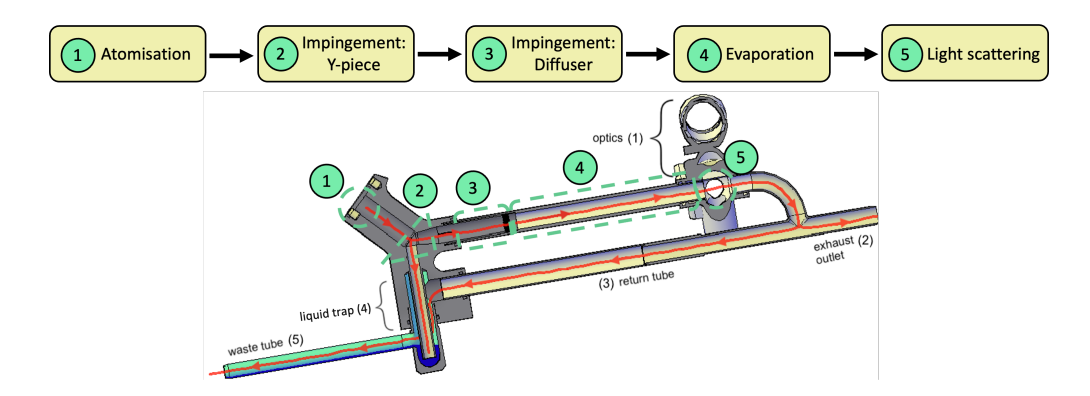


Figure 2. Cross-section of the ELSD detector, indicating inlet, evaporator, outlet, detector, and liquid trap. The unit is assembled with the main ducts at 15 degrees to horizontal to return any liquid droplets to the liquid trap.

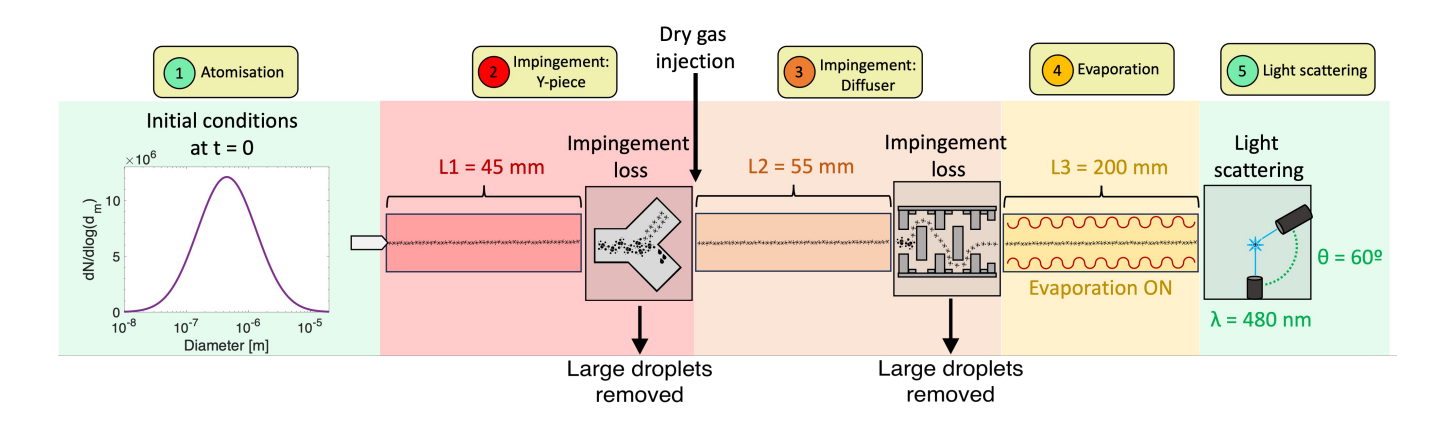


Figure 3. Schematic of the ELSD layout, indicating different elements of the ELSD which affect droplet concentration or size, and represented as separate subsections.

2.3 Nebuliser Sizing experiments

In order to understand the process of droplet evaporation within the flow passages of the ELSD, measurements are required of the particle distribution upstream of the ELSD, *i.e.* the initial droplet size distribution produced from the nebuliser (Figure 1). For the present experiments, the nebuliser was operated at a constant volumetric liquid flow rate of 0.5 mL/min controlled by a syringe pump (Aladdin; SyringeONE AL-1000) and a constant volumetric nitrogen gas flow rate of 0.4 L/min controlled by a mass flow controller (Alicat Scientific).

Upstream particle sizing experiments aim to characterise the droplet size distribution for a given solvent, water, in the case of the aqueous solutions used in later experiments. However, accurately capturing the droplet distribution is particularly challenging due to rapid evaporation of the water solvent. This makes it difficult to obtain in situ measurements that span





the full size range of interest. As a result, multiple complementary techniques are employed to assess the true droplet size distribution as discussed below.

A Phase Doppler Particle Analyser (PDPA; DANTEC Dynamics 2D FiberPDA) was initially used to characterise the droplet size distribution emitted by the nebuliser. The PDPA is a laser-based instrument capable of probing localised spray regions, offering high spatial (sub-millimetre) and temporal (millisecond) resolution. This rapid and localized detection minimises the influence of evaporative losses on the measured droplet size distribution. However, as an optical technique, the PDPA has a lower detection limit of approximately 2 μ m, below which droplets cannot be reliably sized (Boutier, 2013). Consequently, a significant fraction of smaller droplets may fall below the detection threshold and remain unmeasured. To address this limitation, a second instrument was employed to cover the measurement gap between 200 nm and 2 μ m. An Aerodynamic Aerosol Classifier (AAC; Cambustion Ltd.) was used in conjunction with a Condensation Particle Counter (CPC; TSI Instruments Ltd., model 3752) to measure the aerodynamic particle size distribution (Johnson et al., 2018). The latter setup requires sampling, and cannot realize spatially resolved measurements, but it is capable of detecting smaller particles ($\leq 2 \mu$ m). Additionally, droplets that are still evaporating cannot be reliably classified, owing to the long convective time scales involved in sampling lines. A comparison of the capabilities of both instrumentations is provided in Table 2.

Instrument	Size range (µm)	In situ	Evaporating
PDPA	2 - 1000	✓	✓
AAC/CPC	0.200 - 6	×	×

Table 2. Summary of capabilities and drawbacks of the two instruments utilised to elucidate initial droplet distributions.

Preliminary measurements with the PDPA determined that the size peak from the nebuliser lies around the micrometer range. To bridge the measurement gap and approximate the full droplet size distribution, a compromise was achieved by combining PDPA measurements with those from the AAC-CPC system. A series of experiments were conducted using both the PDPA and the AAC/CPC in a size range where both are feasible using a *non-evaporating liquid*, namely dioctyl sebacate (DOS), a low vapour pressure oil (The vapour pressure of DOS is 2.6×10^{-4} Pa at room temperature and pressure, offering negligible evaporation rate (Pence and Williams, 2010)). The solvent properties for both DOS and water are shown in Table 3.

Solvent	Density (kg/m ⁻³)	Surface tension (mN m ⁻¹)
Water	997	72
DOS	914	33.2

Table 3. Solvent physico-chemical properties at standard room temperature and pressure (Pence and Williams, 2010).

Figure 4 shows flow diagrams of the three sets of experiments used to obtain number distribution functions of the original spray.





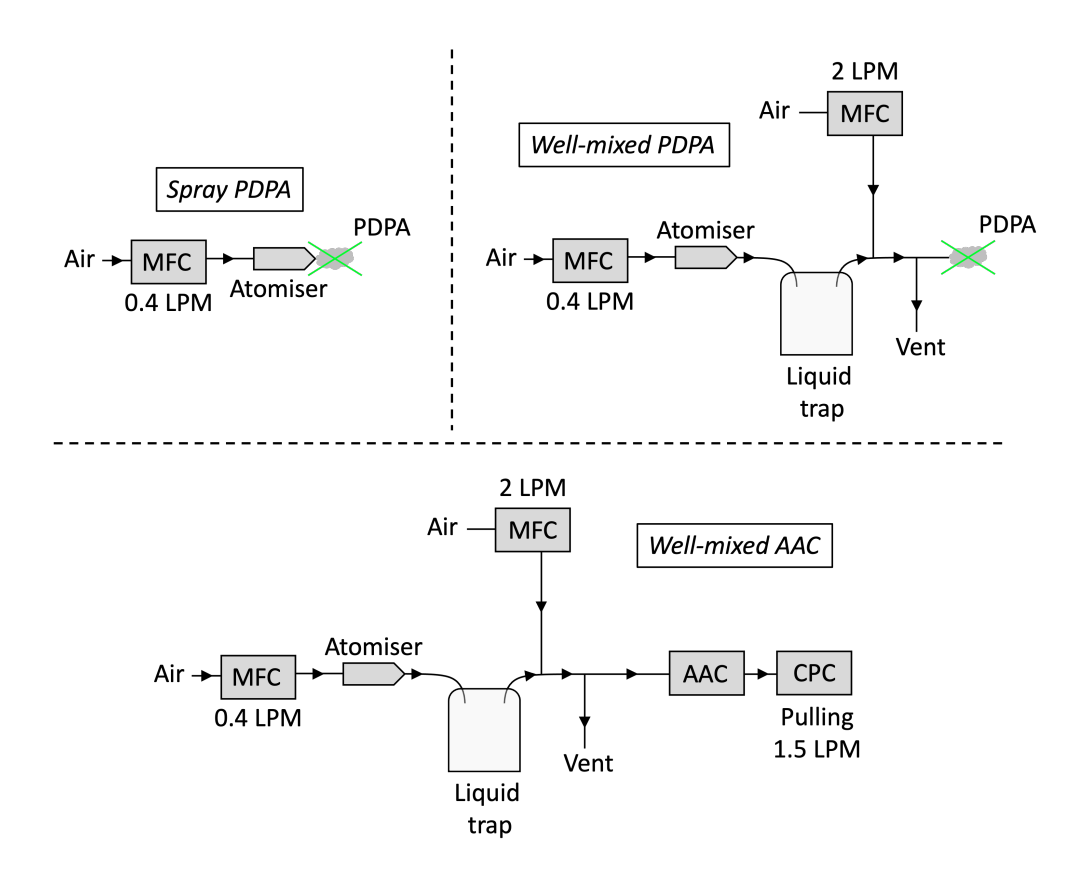


Figure 4. Configurations of the experiments conducted to obtain the initial droplet distribution of DOS. Experiment (1) *Spray PDPA* (top left). Experiment (2) *Well-mixed PDPA* (top right). Experiment (3) *Well-mixed AAC* (bottom).

- 1. Spray PDPA: The PDPA sampling volume is taken within the spray plume at a distance of 1 mm from the tip of the nebuliser along the centreline. The reference droplet size concentration distribution is labeled $n_{P,s}(d_p)$, where d_p is the droplet diameter.
 - 2. Well-mixed PDPA: The atomiser output is collected past a liquid trap and along a tube to a well-mixed outlet. This allows comparison of the integrated, well mixed measurements required by the AAC/CPC setup. The measurements are taken with the PDPA (top right) to yield a size distribution $n_{P,m}(d_p)$.
- 3. Well-mixed AAC: Identical setup as the well-mixed PDPA, but acquired using the AAC/CPC setup as a well-mixed aerosol (bottom), yielding the size distribution $n_{A,m}(d_p)$. Note that the additional air is required for the operation of the AAC/CPC.

In the *well-mixed AAC* experiment, the flow configuration incorporated a liquid trap to eliminate the largest droplets, which is required for preventing the flooding of the instrument, in accordance with the experimental set-up for aerosol generation used by Johnson et al. (2018). Furthermore, this configuration required the inclusion of an additional diluting flow and a vent

Preprint. Discussion started: 18 November 2025

© Author(s) 2025. CC BY 4.0 License.



120

125

130

140

145



to accommodate the required sampling flow rate of the CPC at $1.5 \,\mathrm{L}\,\mathrm{min}^{-1}$, relatively to the atomiser flow of $0.4 \,\mathrm{L}\,\mathrm{min}^{-1}$. The AAC was operated with a sheath flow of $15 \,\mathrm{L}\,\mathrm{min}^{-1}$ and a sample flow of $1.5 \,\mathrm{L}\,\mathrm{min}^{-1}$, corresponding to a resolution (defined as the ratio of particle size to the minimum resolvable size difference) of 10. Under these conditions, the AAC is capable of classifying aerodynamic particle sizes in the range of 200– $6000 \,\mathrm{nm}$. The transfer function of the AAC has been extensively characterised using DOS droplets up to approximately $5 \,\mu\mathrm{m}$ in diameter (Johnson et al., 2018; Payne et al., 2023), and these characterisations were applied in the present study to deconvolve the measured concentrations and recover the underlying particle size distribution.

For the *well-mixed non-evaporative experiment* (*i.e.* (2) and (3) using DOS), particle losses across the liquid trap and transfer tube are attributed to gravitational settling, and adjusted for as outlined in the Appendix. Experimental data from setups (2) and (3) are related via a transfer function, as explained below.

We make the assumption that the particle size distribution from the well-mixed PDPA experiment, $n_{P,m}(d_p)$, should equal that of the well-mixed AAC experiment, $n_{A,m}(d_p)$ above a threshold size (> 2 μ m). However, the values need to be corrected owing to a systematic difference, namely that PDPA measurements measure the passage of droplets at a local sampling volume of the order of a cubic millimetre, whereas the AAC measurements involve sampling the mean integrated total particle number in the flow.

We assume that the differences can be adjusted by a constant factor C, assumed not to be biased across the size distribution, times a transfer function which accounts for the diameter-dependent loss, $f_L(d_p)$ The factor C is obtained by error minimisation across the size distribution obtained with the two measurement methods.

From the comparison between the *well-mixed PDPA* and *well-mixed AAC* experiments it is possible to calculate the loss function associated with the PDPA, f_L , which characterises the diameter dependent signal loss, as given by:

$$n_{P,m}(d_p) = \frac{1}{C} f_L(d_p) n_{A,m}(d_p).$$
(1)

The ratio of the two distributions is calculated as a function of diameter, between $0 < d_p < 2 \mu m$, with the assumption that f_L tends to 1 at sizes larger than 2 μm . A final transfer function, f_T is associated with the losses in the tubes which feed the aerosol into the AAC, which is obtained experimentally by taking the ratio of $spray\ PDPA$, $n_{P,s}(d_p)$, to the well-mixed PDPA experiments:

$$n_{P,s}(d_p) = f_T(d_p) n_{P,m}(d_p).$$
 (2)

It is assumed that all atomised solvents produce a log-normal droplet number distribution:

$$n(d_p) = \frac{N}{d_p \sigma \sqrt{2\pi}} \exp\left(-\frac{\left(\ln d_p - \mu\right)^2}{2\sigma^2}\right),\tag{3}$$

where N is the total concentration of droplets. Log-normal distributions are controlled by the parameters μ and σ , which are analogous to the distribution mode and width, respectively, in logarithmic space. We assume that the mode of the distribution, $\ln \mu$, is obtained from the measurements below 2 μ m using the best fit to the distribution $n_{A,m}$. We also make the assumption that the value of σ does not vary between distributions using different atomising liquids, as its value primarily depends on the





Variable	Minimum value	Maximum value
$\rho (\mathrm{kg m^{-3}})$	800	1220
$\sigma ({ m N m^{-1}})$	0.022	0.072
μ (Pa.s)	0.97×10^{-3}	77.6×10^{-3}

Table 4. Range of physical properties for which Aliseda et al. (2008) provide a correlation.

atomiser geometry (Canals et al., 1988; Kashani and Mostaghimi, 2010). The value of σ is determined from the best fit to $n_{P,s}$ using values above 2 μ m.

In this description, we have so far only considered experiments using a non-evaporating liquid, so that we could use appropriate instrumentation (AAC/CPC) to measure the expected droplet distribution n_{P,m}. However, the liquids used in the ELSD (water, alcohols), have different properties than DOS regarding atomisation. In order to relate the present measurements to those of different fluids, we turn to experiments by Aliseda et al. (2008). Their measurements obtained log-normal distributions for twin-fluid concentric pneumatic nebulisers similar to the one used in the ELSD for this study, for a range of compounds whose physical properties are well within the range of industrially relevant solvents, as shown in Table 4, and obtained a correlation for the Sauter Mean Diameter (SMD, D₃₂) as a function of characteristic flow non-dimensional numbers. The SMD is related to the log-normal parameters μ and σ via (Hinds and Zhu, 2022):

$$D_{32} = \exp\left(\mu + \frac{3}{2}\sigma^2\right). \tag{4}$$

The function linking the D_{32} of the initial droplet distribution to the solvent properties and operating conditions, as expressed in the original work is as follows Aliseda et al. (2008):

$$\frac{D_{32}}{D_L} = C_1 \left(1 + m_r \right) \left(\frac{b_G}{D_L} \right)^{1/2} \left(\frac{\rho_L}{\rho_G \operatorname{Re}_{b_G}} \right)^{1/4} \frac{1}{\sqrt{\operatorname{We}_{D_L}}} \left(1 + C_2 \left(\frac{D_L}{b_G} \right)^{1/6} \left(\frac{\operatorname{Re}_{b_G}}{\rho_L/\rho_G} \right)^{1/12} \operatorname{We}_{D_L}^{1/6} \operatorname{Oh}^{2/3} \right), \tag{5}$$

where D_L is the liquid orifice diameter, b_G is the gas jet thickness (here taken as the thickness of the atomiser gas annulus), ρ_L and ρ_G are densities of the liquid and gas, respectively. Re_G is the gas phase Reynolds number based on the atomizer gas annulus, We_{DL} is the Weber number based on the liquid properties and nozzle diameter, Oh is the Ohnesorge number, and C_1 and C_2 are experimentally determined constants with values of 1.734 and 1.0, respectively. The variable m_r is the liquid to gas mass flow ratio.

The Reynolds number $\operatorname{Re}_{b_G} = \rho_G U_b b_G / \mu_G$ is based on the thickness of the gas annulus and the corresponding gas velocity U_b and dynamic gas viscosity, μ_G . The Weber number is based on the liquid properties of density, ρ_L , and surface tension, σ_L , $\operatorname{We}_{D_L} = \rho_L U_L D_L / \sigma_L$, where the liquid velocity is based on the area defined by the jet diameter, D_L . Finally, the Ohnesorge number is also based on the liquid properties and jet diameter, $\operatorname{Oh} = \mu_L / \sqrt{\rho_L \sigma_L D_L}$.



190



The final step is to obtain the actual number concentrations in the flow (coming from the atomiser centreline) for the particular operating conditions. These are obtained from imposing the conservation of liquid volumetric flow rate for the droplets, starting from the droplet size concentration distribution $n_{P,s}$, which is assumed to remain self-similar for different fluids:

175
$$Q_L = \phi Q_G \int_0^\infty n_{P,s}(d_p) \frac{\pi}{6} d_p^3 d(d_p)$$
 (6)

where Q_L and Q_G are the measured volumetric flow rates of liquid and gas delivered to the injector at reference conditions, the integral obtained corresponds to the total liquid mass per unit volume of gas, and the correction factor ϕ is applied to obtain the final estimated input droplet number distribution of the mixture of solvent and dilute analyte delivered by the nebuliser at section (1).

180 2.4 ELSD outlet particle sizing experiments

The previous section detailed the steps taken to obtain the particle size distributions at the upstream end of the detector, which acts as an input to the overall model (*i.e.* (1) in Figure 3). In order to verify the accuracy of a model, it is also necessary to obtain particle size distributions at the outlet of the ELSD detector (*i.e.* corresponding to the outlet of (4) in Figure 3).

The measurements are made using a Scanning Mobility Particle Sizer (SMPS, TSI Instruments Ltd.). The SMPS comprises two pieces of aerosol instrumentation in series: a Differential Mobility Analyser (DMA) and a CPC. The outlet of the ELSD was connected via non-particle generating, conductive rubber tubing to the inlet of the SMPS as shown in Figure 5. All SMPS experiments in this study used TSI-made DMAs (electrostatic classifier models 3080 and 3082 and a model 3081 long column) and CPCs (models 3752 and 3776).. The SMPS was operated with a negative polarity such that positively charged particles were selected, with an aerosol flow of 1.5 L min⁻¹ and a sheath flow 15 L min⁻¹. Experiments were obtained over 90-second scans across the explored size range of 8 to 232 nm. Each set of experimental conditions were repeated 3 times to ensure reproducibility; the reported results show the average of these 3 runs for each case.

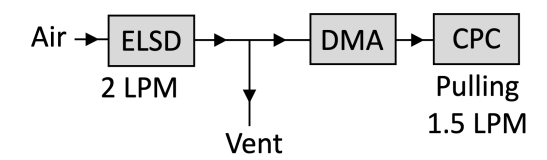


Figure 5. Configuration for the acquisition of particle size distribution downstream of the ELSD. The DMA and CPC make up the SMPS.

2.5 SEM images

Samples were collected from the ELSD outlet for SEM analysis onto carbon TEM grids (EM Resolutions, Holey Carbon Film, Cu, 300 mesh, 4-6 nm, UL, hole diameters ranging from 0.25 to 5 µm, for 3 minutes using an ELSD gas flow of 2 L min⁻¹.



195 The samples were coated in platinum to ensure that the organic samples were electrically conductive enough to be visible in the SEM before being analysed on a TESCAN MIRA3 FEG-SEM at 5 kV.

3 Results and discussion

3.1 Upstream droplet size measurements

Results of the particle size distribution measurements obtained as described in Section 2.3 from the PDPA and AAC experi-200 ments using DOS are shown in Figure 6.

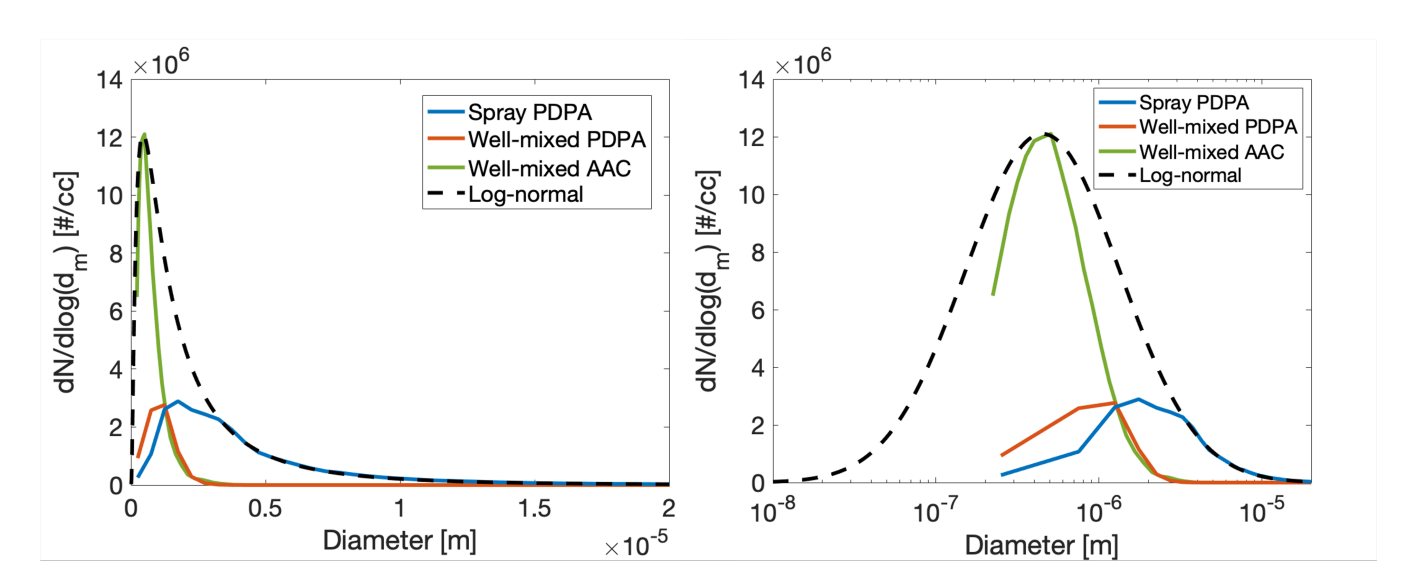


Figure 6. Normalised particle size distributions for non-evaporating DOS droplets measured downstream of the atomiser. Distributions shown correspond to Spray PDPA, $n_{\rm P,s}$ (obtained directly from the PDPA atomizer centreline), Well-mixed PDPA $n_{\rm P,m}$ (obtained from the well-mixed setup), Well-mixed AAC $n_{\rm A,m}$ (obtained from the well-mixed setup). The black dashed line shows a log-normal fit obtained according to the procedure described in the text: the mode from the well-mixed AAC, and the σ from the Spray PDPA. Left plot shown with diameter as a linear scale (left) and as a log-normal scale (right).

The green line for the well-mixed AAC measurements shows a log-normal mode around 450 nm, which is adopted as the mode for the final original spray distribution. The orange line for well-mixed PDPA, $n_{P,m}$ shows good agreement with the well-mixed AAC green $n_{A,m}$ line once scaled by a best fit factor $f_L(d_P)/C$. The spray PDPA blue line is scaled by the same factor $f_L(d_P)/C$. The ratio of the blue signal (spray PDPA) and orange signal (well-mixed PDPA) reflects the losses within the liquid trap and tube via f_T . The values determined for f_T and f_L as a function of diameter are shown in Fig. 7. The best fit log-normal curve for the final total spray concentration curve $n_{P,s}(d_p)$ is shown as the black dashed-line log-normal curve in Fig. 6. The procedure can be summarised as using the mode determined by the AAC measurements and the value of σ determined by the Spray PDPA measurements.





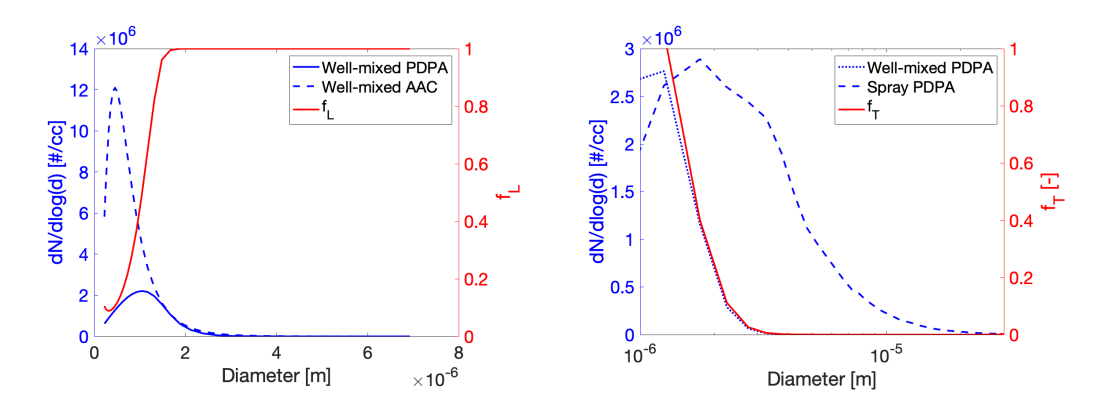


Figure 7. Loss function, f_L , and transfer function, f_T , as obtained from experimental data. (left) f_L superimposed on the distributions obtained via well-mixed cases, (right) f_T superimposed on the distributions obtained via PDPA experiments. Logarithmic scale for diameter.

Once the mode and σ for the DOS distribution are determined, the correlation in Eq. 5 was used to determine the expected value of D_{32} , and thus an updated value of μ , assuming that σ remains constant, and that the total volume flow rate is conserved, as expressed in Eq. 6. The original distribution for DOS and the final result for the expected droplet number distribution for water from the nebuliser is shown in Fig. 8.

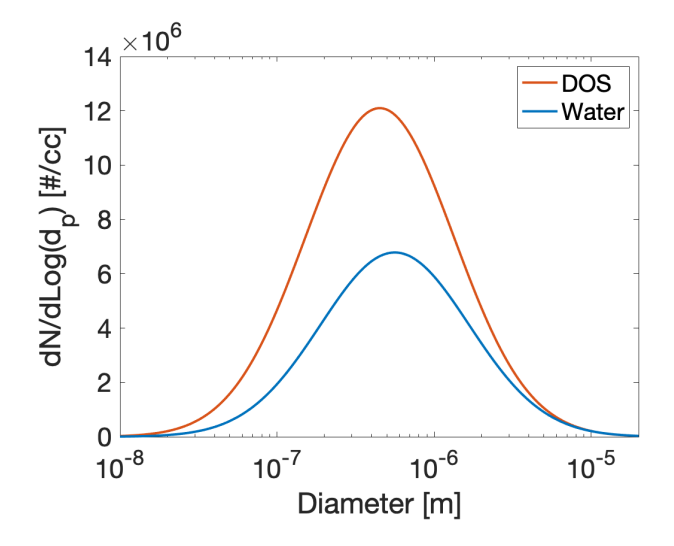


Figure 8. Initial droplet distributions for DOS (mode = 450 nm, σ = 1.08) and water (mode = 550 nm, σ = 1.08) on a logarithmic scale.

The initial size distribution of water droplets is approximated using the same liquid and gas volumetric flow rates as in the DOS case. As a result, by conservation of volume, a larger peak droplet diameter corresponds to a lower peak number concentration compared to DOS. This difference in peak diameter is due to the higher surface tension of water relative to DOS.





An increased surface tension would lead to more energy being required to break the liquid jet into droplets, resulting in larger droplets overall.

3.2 Particle size measurements downstream of evaporator and detector tube

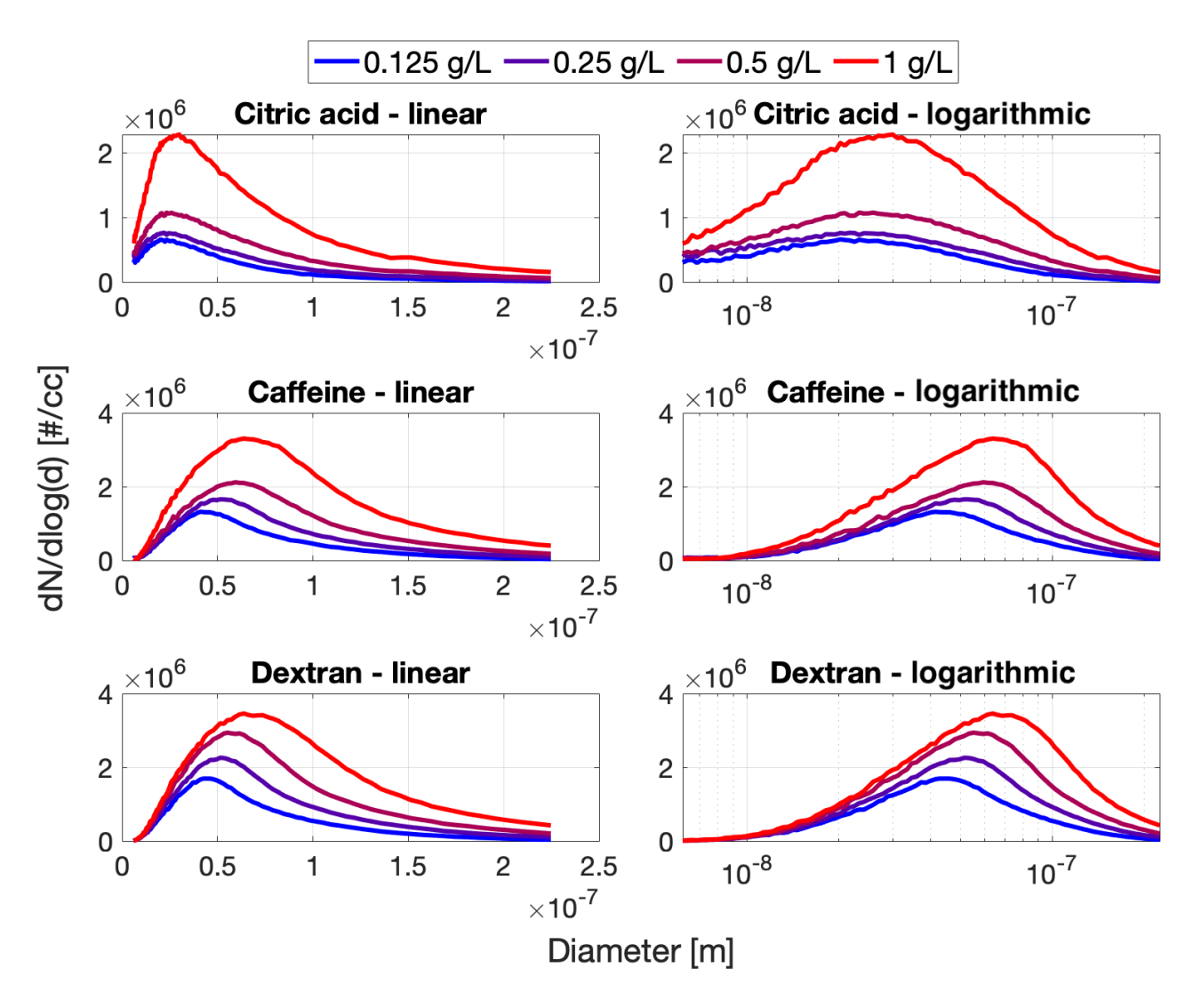


Figure 9. Mobility diameter SMPS scans of citric acid (top row), dextran (middle row), and caffeine (bottom row) injections through the ELSD at 25 °C for different initial analyte concentrations; mobility diameter shown as a linear scale (left) and as a log-normal scale (right).

Measurements of particle concentrations as a function of size emerging from the evaporator section were made using an SMPS, and are shown in Fig. 9 for caffeine, dextran, and citric acid diluted in water at concentrations from 0.125 to $1~{\rm g~L^{-1}}$. Analytes with different volatilities and bulk densities were selected to understand whether different particle size distributions

Preprint. Discussion started: 18 November 2025

© Author(s) 2025. CC BY 4.0 License.



225

230

250

255



are produced. Their properties are shown in Table 1, with the lowest volatility associated with citric acid, followed by caffeine. The volatility of dextran is not known, although its molecular weight is highest compared to the other two compounds.

The lowest overall concentrations and smallest mean diameters are associated with citric acid, which has lower volatility and higher effective density relatively to caffeine. Although there is little information about dextran properties, measurements show very little systematic difference between the number distributions compared to caffeine. This may indicate similar effective densities upon drying.

As expected, the peak numbers increase with the concentration, but not linearly across the range. For all cases, the mode of the distribution increases with concentration. One can also observe that the log-normal distribution is not symmetric, but rather skewed towards larger sizes. This is indicative of a distribution which has gone through a size-dependent impingement via a cut-off diameter. This can be attributed to the effects of the Y-junction and the diffuser cartridge (sections 2 and 3 in Figure 3) on the aerosol. Further evidence is presented in the parallel study modelling the ELSD signal response, which demonstrates that a collection-efficiency curve for the two aforementioned impingement points leads to such a skewed distribution Bertani et al. (2025).

From the measurements and adjustments discussed for the nebulised droplet distribution, a number concentration peak at a diameter value of 550nm and a peak width of $\sigma = 1.08$ is estimated for the reconstructed initial distribution of water (Figure 8). An estimate of the dried particle size for a droplet of initial diameter d_0 , of analyte mass concentration c in the liquid can be made by assuming that the mass m_a of the analyte not captured by the impingement is conserved after all solvent water has evaporated, leaving a final spherical droplet diameter d_f with known bulk density ρ_b :

240
$$m_a = \frac{\pi}{6} d_0^3 c = \frac{\pi}{6} d_f^3 \rho_b,$$
 (7)

The estimated diameter d_f obtained can be thought of as a lower bound for the dried particle diameter, as the bulk density may differ from that of the dried particle, particularly as the dried particle diameter may differ from a sphere. Assuming that we can compare the peak of the distributions, we can compare the mode of the initial droplet distribution with the mode of the SMPS distribution:

245
$$d_f = d_0 \left(\frac{c}{\rho_b}\right)^{1/3}$$
, (8)

Substituting the values for effective density values for the bulk density values given on Tables 1 and Tables 3, and using the mode diameters from the peaks of Fig. 9, yields final mode diameters of 46 nm and 52 nm for citric acid and caffeine respectively. The resulting values should be compared to the measured modes of 35 nm 65 nm, respectively, according to values on Fig. 9. The estimated values generally align with the experimental measurements; however, the value for citric acid is over-predicted, while caffeine is under-predicted. The under-prediction of the peak caffeine diameter indicates a lower effective density of caffeine particles compared to than the bulk value; this is consistent with the SEM results shown in the next section, as the collected dried caffeine samples are not spherical in shape. The over-prediction of the peak citric acid diameter may be attributed to inaccuracies associated with the construction of the initial droplet distribution of water and possible mixing effects reducing the surface tension of the water-citric acid solution and changing the diameter; a decreased surface tension is consistent with less energy required to break the liquid jet into droplets, resulting in smaller droplets overall.





3.3 SEM images

SEM images were collected for the three analytes selected on Table 1, according to methodology described in the experimental methods section 2.5. The efficiency of the collection grids used for SEM imaging reach minimum efficiencies below 20% in the size range of 5–300 nm (Xiang et al., 2021). Therefore, whereas the images can be analysed for particle size distribution, they are only representative for particles larger than 300 nm. Here we present SEM images to gain insight into the morphology of dried particles in the ELSD, and to what extent particle shape might affect the scattering properties which directly lead to light detection.

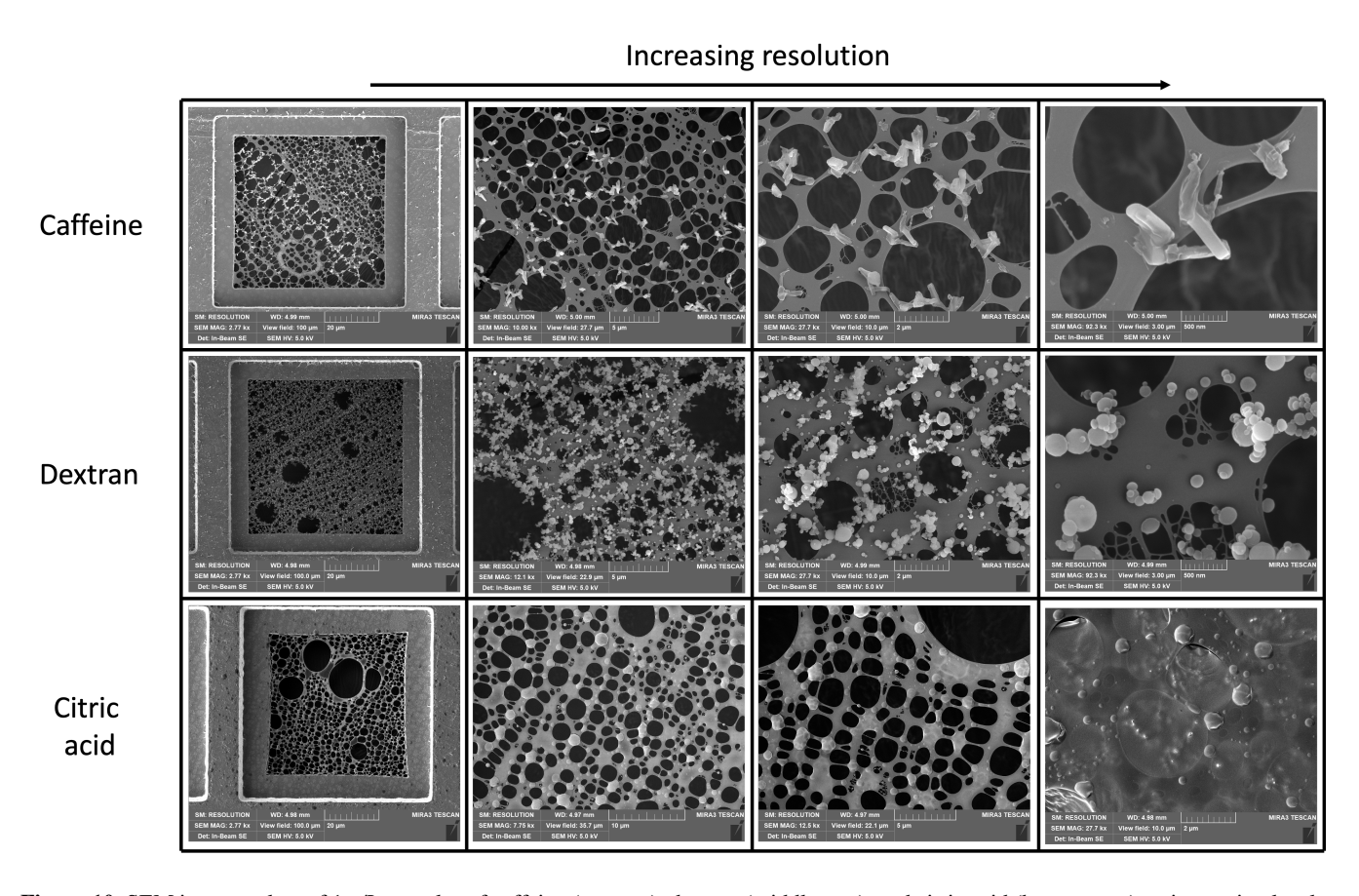


Figure 10. SEM images taken of 1 g/L samples of caffeine (top row), dextran (middle row), and citric acid (bottom row), at increasing levels of magnification.

Figure 10 shows SEM images of grids with collected particles for the three selected analytes at the same operating condition for caffeine, dextran and citric acid, in order of increasing spatial resolution. Caffeine samples produced particles with a notably elongated morphology, with a few shorter particles with crystalline character. This is consistent with literature reports of caffeine crystallising into needles in bulk (Sarfraz et al., 2012). This finding may have significant consequences for the

https://doi.org/10.5194/ar-2025-35

Preprint. Discussion started: 18 November 2025

© Author(s) 2025. CC BY 4.0 License.



270

275

280

285

AEROSOL Research

detection of caffeine via light-scattering since the morphology found via SEM differs significantly from that of a sphere. Dextran produced spherical particles with an approximately spherical morphology with a large variety of diameters, as shown in Figure 10. These are often agglomerated into larger particles with different primary particle sizes. This is also consistent with literature reports for dried dextran particles (Yuan et al., 2007). Finally, samples of citric acid produced particles which are approximately spherical, and not agglomerated. Particles tended to collect in the regions around the holes of the TEM grid. This suggests that the citric acid particles may have particular surface tension properties associated with liquids (possibly water) as they were deposited onto the TEM grids. This is in contrast to available literature on bulk drying of aqueous citric acid, which suggests that citric acid formed crystals with distinct networks of multi-layer agglomerates (Ohgaki et al., 1992; Ueda et al., 1995; Groen and Roberts, 2001). The difference may suggest that there is a different in crystallization in bulk compared to atomized droplets.

4 Conclusions

This study provides a comprehensive characterization of particle formation and evolution within the ELSD. By combining multiple particle sizing techniques and SEM imaging, we have elucidated the complex relationships between initial droplet formation, solvent evaporation, and final particle morphology for different analytes. Our results demonstrate that the initial droplet size distribution can be approximated using non-evaporating surrogates and correlated to aqueous solutions. Downstream measurements reveal that analyte properties, particularly volatility and bulk density, significantly influence final particle size distributions. SEM images further highlight the diverse morphologies of dried particles, ranging from elongated caffeine crystals to spherical dextran agglomerates and approximately spherical citric acid particles.

These findings form the database for understanding ELSD functioning and detection mechanisms in order to optimize performance across different analytes. The observed differences in particle size and morphology can contribute to variations in light scattering behaviour, which directly impacts detector response. A companion paper develops a model for eluent atomization and drying, and uses the present results for validation.

The outlook of the combined experiments and model allows the development of improved instrument designs and more robust analytical methods for a wide range of applications of the ELSD in pharmaceutical, biomaterials, and food science research.

Data availability. The dataset associated with this article can be made available from the corresponding author on request.

© Author(s) 2025. CC BY 4.0 License.





Appendix A: Loss calculations

A1 Diffusional losses

The loss of particles due to diffusion was calculated via the Gormley and Kennedy equation for aerosol penetration, P, in a tube as given by Hinds Hinds and Zhu (2022):

$$P = \begin{cases} 1 - 5.5\chi^{2/3} + 3.77\chi & \chi < 0.009\\ 0.819 \exp(-11.5\chi) + 0.0975 \exp(-70.1\chi) & \chi \ge 0.009 \end{cases}$$
(A1)

where χ is the penetration parameter, and is expressed as the ratio of a diffusive to convective velocity:

$$\chi = \frac{\mathcal{D}L}{Q_q},\tag{A2}$$

where L is the tube length, Q is the gas volumetric flow-rate, and \mathcal{D} is the mass diffusivity of the aerosol in the fluid as given by:

$$\mathcal{D} = \frac{k_B T C_c}{3\pi \mu_o d},\tag{A3}$$

In the equation above, C_c is the Cunningham slip correction factor and is given by:

$$C_c = 1 + \frac{\lambda}{d} \left(2.34 + 1.05 \exp\left(-0.39 \frac{d}{\lambda} \right) \right),\tag{A4}$$

305 where λ is the gas mean free path.

By taking the length of the tube as 2 metres, and the gas flow rate as $2 L min^{-1}$, and applying equation (A1) to a variety of diameters the diameter-dependent value of P is shown in figure A1.

From Figure A1, it is observed that the penetration value increases with particle size, reaching values greater than 99% penetration for particles of 100 nm and above. Thus, it was concluded that diffusional loss was negligible in the determination of the initial particle distribution.

A1 Gravitational losses

The loss of large particles from the point of atomisation to the point where the particles can first be detected with the AAC can also be rationalised by calculating the expected losses with the gravitational velocity, V_{gv} , for particles of this size. Hinds and Zhu (2022):

315
$$V_{gv} = \frac{(\rho_p - \rho_g) d_p^2 g}{18\mu_g},$$
 (A1)

where q is the acceleration due to gravity. In the case of DOS atomisation this simplifies to:

$$V_{gv} = 2.74 \cdot 10^7 d_p^2, \tag{A2}$$





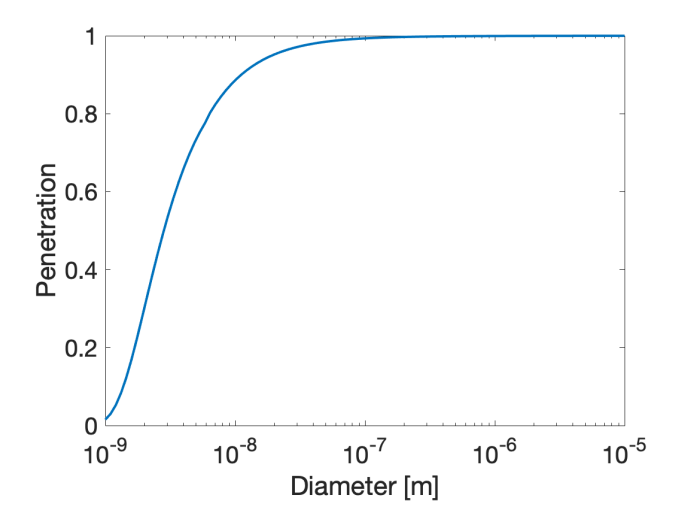


Figure A1. Values for aerosol penetration for a range of diameters, given the conditions in the well-mixed experiments.

where all variables are given in S.I. units.

The piping used to connect the atomiser to the AAC was a $\frac{1}{4}$ inch internal diameter tube, with an internal radius $R=320~3.175\cdot 10^{-3}~\mathrm{m}$, and cross-sectional area of $3.17\cdot 10^{-5}~\mathrm{m}^2$. Since the atomiser was the only source of gas flow, at $0.4~\mathrm{L~min^{-1}}$, this is equivalent to a mean flow speed of $V=0.21~\mathrm{m~s^{-1}}$, or a total flow time $t=9.5~\mathrm{s}$ for a tube around 2 m in length. The penetration depth can be found by equating the limit setting velocity to the convective velocity, and solving for the cut-off diameter of $3.5~\mathrm{\mu m}$. The limit can explain the difference between the original PDPA distribution and the value with the well-mixed AAC, which contains very low number concentrations of particles above $3.5~\mathrm{\mu m}$.

https://doi.org/10.5194/ar-2025-35 Preprint. Discussion started: 18 November 2025 © Author(s) 2025. CC BY 4.0 License.





325 *Author contributions.* CRediT: F. Bertani: Data curation, Investigation, Writing – original draft, Formal analysis. J. Hassim: Methodology, Investigation, Resources. S. Hochgreb: Conceptualization, Supervision, Funding acquisition.

Competing interests. There are no known competing interests.

Acknowledgements. F. Bertani and J. Hassim were funded by the UK EPRSC Centre for Doctoral Training in Aerosol Science (EP/S023593/1).

F. Bertani was partly funded by Agilent, Inc. (S. O'Donohue, S. Bullock, Grant 4414), and J. Hassim was partly funded by Alphasense, with
a further contribution from Cambustion. An HPLC/ELSD prototype was loaned from Agilent for the experimental work. We also thank Prof.
A. Boies for the shared aerosol measurement equipment. For the purpose of open access, the authors have applied a Creative Commons
Attribution (CC BY) licence to any Author Accepted Manuscript version arising from this submission.





References

365

- Adelantado, C. et al.: Analysis of silica nanoparticles by capillary electrophoresis coupled to an evaporative light scattering detector, Analytica Chimica Acta, 923, 82–88, 2016.
 - Aliseda, A., Hopfinger, E. J., Lasheras, J. C., Kremer, D. M., Berchielli, A., and Connolly, E. K.: Atomization of viscous and non-Newtonian liquids by a coaxial, high-speed gas jet. Experiments and droplet size modeling, International Journal of Multiphase Flow, 34, 161–175, 2008.
- Bertani, F., Hassim, J., and Hochgreb, S.: Simulating aerosol dynamics and signal response in the Evaporative Light Scattering Detector,

 Aerosol Research, 2025.
 - Boborodea, A., Mirabella, F. M., and O'Donohue, S.: Polyolefin characterization in xylene by high-temperature gel permeation chromatography with a new evaporative light scattering detector, Chromatographia, 81, 419–424, 2018.
 - Bothe, H. and Cammenga, H. K.: Phase transitions and thermodynamic properties of anhydrous caffeine, Journal of Thermal Analysis, 16, 267–275, https://doi.org/10.1007/BF01910688, 1979.
- Boutier, A.: Laser metrology in fluid mechanics: granulometry, temperature and concentration measurements, John Wiley & Sons, 2013.
 - Cai, C. et al.: Organic component vapor pressures and hygroscopicities of aqueous aerosol measured by optical tweezers, The Journal of Physical Chemistry A, 119, 704–718, https://doi.org/10.1021/jp510525r, 2015.
 - Canals, A. et al.: Empirical model for estimating drop size distributions of aerosols generated by inductively coupled plasma nebulizers, Spectrochimica Acta Part B: Atomic Spectroscopy, 43, 1321–1335, https://doi.org/10.1016/0584-8547(88)80172-1, 1988.
- Dalavitsou, A. et al.: Analytes' Structure and Signal Response in Evaporating Light Scattering Detector (ELSD), Current Analytical Chemistry, 15, 540–552, 2019.
 - Doß, M. and Bänsch, E.: Numerical study of single droplet drying in an acoustic levitator before the critical point of time, Chemical Engineering Science, 248, 117 149, https://doi.org/10.1016/j.ces.2021.117149, 2022.
- Fu, N., Woo, M. W., and Chen, X. D.: Single droplet drying technique to study drying kinetics measurement and particle functionality: a review, Drying Technology, 30, 1771–1785, https://doi.org/10.1080/07373937.2012.708002, 2012.
 - Gregson, F. K. A. et al.: Drying kinetics of salt solution droplets: Water evaporation rates and crystallization, The Journal of Physical Chemistry B, 123, 266–276, https://doi.org/10.1021/acs.jpcb.8b09584, 2018.
 - Griesser, U. J., Szelagiewicz, M., Hofmeier, U. C., et al.: Vapor Pressure and Heat of Sublimation of Crystal Polymorphs, Journal of Thermal Analysis and Calorimetry, 57, 45–60, https://doi.org/10.1023/A:1010188923713, 1999.
- 360 Groen, H. and Roberts, K. J.: Nucleation, growth, and pseudo-polymorphic behavior of citric acid as monitored in situ by attenuated total reflection Fourier transform infrared spectroscopy, The Journal of Physical Chemistry B, 105, 10723–10730, https://doi.org/10.1021/jp0111281, 2001.
 - Hinds, W. C. and Zhu, Y.: Aerosol technology: properties, behavior, and measurement of airborne particles, John Wiley & Sons, 2022.
 - Johnson, T. J., Irwin, M., Symonds, J. P. R., Olfert, J. S., and Boies, A. M.: Measuring aerosol size distributions with the aerodynamic aerosol classifier, Aerosol Science and Technology, 52, 655–665, https://doi.org/10.1080/02786826.2018.1440063, 2018.
 - Kashani, A. and Mostaghimi, J.: Aerosol characterization of concentric pneumatic nebulizer used in inductively coupled plasma—Mass spectrometry (ICP-MS), Atomization and Sprays, 20, 2010.
 - Lafosse, M. et al.: The advantages of evaporative light scattering detection in pharmaceutical analysis by high performance liquid chromatography and supercritical fluid chromatography, Journal of High Resolution Chromatography, 15, 312–318, 1992.





- Liu, W. et al.: Segregation in drying binary colloidal droplets, ACS Nano, 13, 4972–4979, https://doi.org/10.1021/acsnano.9b00459, 2019.
 - Mourey, T. H. and Oppenheimer, L. E.: Principles of operation of an evaporative light-scattering detector for liquid chromatography, Analytical Chemistry, 56, 2427–2434, 1984.
 - Ohgaki, K., Hirokawa, N., and Ueda, M.: Heterogeneity in aqueous solutions: electron microscopy of citric acid solutions, Chemical Engineering Science, 47, 1819–1823, https://doi.org/10.1016/0009-2509(92)80300-2, 1992.
- Payne, S. D., Johnson, T. J., and Symonds, J. P. R.: Characterisation of the Aerodynamic Aerosol Classifier Transfer Function for Particle Sizes up to 5 Micrometres, Aerosol and Air Quality Research, 23, 230 008, https://doi.org/10.4209/aagr.230008, 2023.
 - Pence, H. E. and Williams, A.: ChemSpider: an online chemical information resource, 2010.
 - Power, R. M. and Reid, J. P.: Probing the micro-rheological properties of aerosol particles using optical tweezers, Reports on Progress in Physics, 77, 074 601, https://doi.org/10.1088/0034-4885/77/7/074601, 2014.
- 380 Sarfraz, A. et al.: Morphological diversity of caffeine on surfaces: needles and hexagons, Crystal Growth & Design, 12, 583–588, https://doi.org/10.1021/cg101358q, 2012.
 - Sungkhaphaitoon, P., Wisutmethangoon, S., and Plookphol, T.: Influence of process parameters on zinc powder produced by centrifugal atomisation, Materials Research, 20, 718–724, https://doi.org/10.1590/1980-5373-MR-2015-0674, 2017.
 - Ueda, M. et al.: Change in microstructure of an aqueous citric acid solution under crystallization, Journal of Crystal Growth, 156, 261–266, https://doi.org/10.1016/0022-0248(95)00298-7, 1995.
 - Urionabarrenetxea, E. et al.: Experimental study of the influence of operational and geometric variables on the powders produced by close-coupled gas atomisation, Materials & Design, 199, 109 441, https://doi.org/10.1016/j.matdes.2020.109441, 2021.
 - Wulsten, E. et al.: Levitated single-droplet drying: Case study with itraconazole dried in binary organic solvent mixtures, International Journal of Pharmaceutics, 378, 116–121, https://doi.org/10.1016/j.ijpharm.2009.05.060, 2009.
- 390 Xiang, M. et al.: Airborne nanoparticle collection efficiency of a TEM grid-equipped sampling system, Aerosol Science and Technology, 55, 526–538, 2021.
 - Yuan, W., Wu, F., Geng, Y., Xu, S., and Jin, T.: Preparation of dextran glassy particles through freezing-induced phase separation, International Journal of Pharmaceutics, 339, 76–83, https://doi.org/10.1016/j.ijpharm.2007.02.018, 2007.